

An extreme [O III] emitter at $z = 3.2$: a low metallicity Lyman continuum source

S. de Barros¹, E. Vanzella¹, R. Amorín², M. Castellano², B. Siana³, A. Grazian², H. Suh^{4,8}, I. Balestra⁵, C. Vignali^{1,6},
A. Verhamme⁷, G. Zamorani¹, M. Mignoli¹, G. Hasinger⁸, A. Comastri¹, L. Pentericci², E. Pérez-Montero⁹,
A. Fontana⁴, M. Giavalisco¹⁰, and R. Gilli¹

¹ INAF–Osservatorio Astronomico di Bologna, via Ranzani 1, I-40127 Bologna, Italy, email: stephane.debarros@oabo.inaf.it

² INAF–Osservatorio Astronomico di Roma, via Frascati 33, 00040 Monteporzio, Italy

³ Department of Physics and Astronomy, University of California, Riverside, CA 92507, USA

⁴ Harvard-Smithsonian Center for Astrophysics, Cambridge, MA 02138, USA

⁵ INAF–Osservatorio Astronomico di Trieste, via G. B. Tiepolo 11, 34131, Trieste, Italy

⁶ Dipartimento di Fisica e Astronomia, Università degli Studi di Bologna, Viale Berti Pichat 6/2, 40127 Bologna, Italy

⁷ Observatoire de Genève, Université de Genève, Ch. des Maillettes 51, 1290 Versoix, Switzerland

⁸ Institute for Astronomy, 2680 Woodlawn Drive, Honolulu, Hawaii 96822, USA

⁹ Instituto de Astrofísica de Andalucía, CSIC, Apartado de correos 3004, 18080 Granada, Spain

¹⁰ Astronomy Department, University of Massachusetts, Amherst, MA 01003, USA

Received ; accepted

ABSTRACT

Aims. The cosmic reionization is an important process occurring in the early epochs of the Universe. However, because of observational limitations due to the opacity of the intergalactic medium to Lyman continuum photons, the nature of ionizing sources is still not well constrained. While high-redshift star-forming galaxies are thought to be the main contributors to the ionizing background at $z > 6$, it is impossible to directly detect their ionizing emission. Therefore, looking at intermediate redshift analogues ($z \sim 2 - 4$) can provide useful hints about cosmic reionization.

Methods. We investigate the physical properties of one of the best Lyman continuum emitter candidate at $z = 3.212$ found in the GOODS-S/CANDELS field with photometric coverage from U to MIPS $24\mu\text{m}$ band and VIMOS/VLT and MOSFIRE/Keck spectroscopy. These observations allow us to derive physical properties such as stellar mass, star-formation rate, age of the stellar population, dust attenuation, metallicity, and ionization parameter, and to determine how these parameters are related to the Lyman continuum emission.

Results. Investigation of the UV spectrum confirms a direct spectroscopic detection of the Lyman continuum emission with $S/N > 5$. Non-zero $\text{Ly}\alpha$ flux at the systemic redshift and high Lyman- α escape fraction ($f_{\text{esc}}(\text{Ly}\alpha) \geq 0.78$) suggest a low H I column density. The weak C and Si low-ionization absorption lines are also consistent with a low covering fraction along the line of sight. The sub-solar abundances are consistent with a young and extreme starburst. The $[\text{O III}]\lambda\lambda 4959, 5007 + \text{H}\beta$ equivalent width (EW) is one of the largest reported for a galaxy at $z > 3$ ($\text{EW}([\text{O III}]\lambda\lambda 4959, 5007 + \text{H}\beta) \approx 1600\text{\AA}$, rest-frame; 6700\AA observed-frame) and the NIR spectrum shows that this is mainly due to an extremely strong $[\text{O III}]$ emission. The large observed $[\text{O III}]/[\text{O II}]$ ratio (> 10) and high ionization parameter are consistent with prediction from photoionization models in case of a density-bounded nebula scenario. Furthermore, the $\text{EW}([\text{O III}]\lambda\lambda 4959, 5007 + \text{H}\beta)$ is comparable to recent measurements reported at $z \sim 7 - 9$, in the reionization epoch. We also investigate the possibility of an AGN contribution to explain the ionizing emission but most of the AGN identification diagnostics suggest that stellar emission dominates instead.

Conclusions. This source is currently the first high- z example of a Lyman continuum emitter exhibiting indirect and direct evidences of a Lyman continuum leakage and having physical properties consistent with theoretical expectation from Lyman continuum emission from a density-bounded nebula. A low H I column density, low covering fraction, compact star-formation activity, and a possible interaction/merging of two systems may contribute to the Lyman continuum photon leakage.

Key words. Galaxies: high-redshift; Galaxies: evolution; Galaxies: ISM; Galaxies: starburst

1. Introduction

One of the most pressing, unanswered questions in cosmology and galaxy evolution is which are the sources responsible for the reionization of the intergalactic medium (IGM; Robertson et al. 2015) and capable of keeping it ionized afterwards (Fontanot et al. 2014; Giallongo et al. 2015). Until recently, it was difficult to draw a consistent picture based on the different observational constraints (e.g., reconciling the ionizing background and the galaxy UV luminosity density; Bouwens et al. 2015). However, there is still a large number of unconstrained param-

eters at $z > 6$, the most important one probably being the Lyman continuum escape fraction ($f_{\text{esc}}(\text{LyC})$; Zackrisson et al. 2013). Unfortunately, it is not possible to directly detect Lyman continuum emission at the epoch of reionization or even in the aftermath (e.g., at any redshift $z > 4.5$), due to the very high cosmic opacity (e.g., Worseck et al. 2014).

A number of surveys at $1 < z < 3.5$ both from the ground and with the Hubble Space Telescope (*HST*), have looked for ionizing photons by means of imaging or spectroscopy and there have been some claims of detections (Steidel et al. 2001; Shapley et al. 2006; Nestor et al. 2013; Mostardi et al. 2013, 2015).

However, careful analysis of some claims combining different instruments (e.g., near-infrared spectroscopy and high spatial resolution probing LyC, Siana et al. 2015) shows that the individual detections must be considered with caution because of the difficulty to eliminate a possible foreground contamination (Vanzella et al. 2010b; Mostardi et al. 2015). Several other surveys reported only upper limits (Siana et al. 2010; Bridge et al. 2010; Malkan et al. 2003; Vanzella et al. 2010b, 2012; Boutsia et al. 2011; Grazian et al. 2015). This could be due to the rarity of relatively bright ionizing sources, as a consequence of the combination of view-angle effects (Cen & Kimm 2015), stochastic intergalactic opacity (Inoue & Iwata 2008; Inoue et al. 2014) and possibly intrinsically low escaping ionizing radiation on average, in the luminosity regime explored so far ($L > 0.1L^*$, e.g., Vanzella et al. 2010b).

At higher redshifts, the galaxy contribution to the cosmic ionization budget must be inferred from other properties that correlate with their ability to contribute to ionizing radiation, if such properties exist. This is an open line of research with ground and space-based facilities. Indirect signatures in the non-ionizing domain have been investigated by performing photoionization and radiative transfer modeling. Low column density and covering fraction of neutral gas (that regulate the escape fraction of ionizing radiation) are related to a series of possible indicators:

1. the nebular conditions, (i.e. density-bounded or radiation bounded) traced by peculiar line ratios like large [O III]/[O II] ratio (e.g., Jaskot & Oey 2014; Nakajima & Ouchi 2014) or deficit of Balmer emission lines given the inferred star-formation rate (SFR) and the UV β slope ($F_\lambda \propto \lambda^\beta$; Zackrisson et al. 2013);
2. strength of interstellar absorption lines as a trace of neutral gas covering fraction (Jones et al. 2012; Heckman et al. 2011);
3. structure of the Ly α emission line, its width and position relative to the systemic redshift (e.g., Verhamme et al. 2015);
4. morphology and spatial distribution of the star formation activity (e.g., nucleation) which seems to be another property that favors efficient feedback and eventually a transparent medium for ionizing radiation (e.g., Heckman et al. 2011; Borthakur et al. 2014).

While all these features are promising signatures, possibly usable at the redshifts of the reionization, there is still a missing direct link between them and the Lyman continuum emission. In this respect there is an ongoing effort to investigate this possible link in a particular class of sources that seem to possess all the above properties. The idea is to look for “green pea” (GP) galaxies in the nearby Universe. GPs have been discovered in the Galaxy Zoo project (Cardamone et al. 2009). They are small compact galaxies in the SDSS survey at $0.11 < z < 0.36$, dominated by strong [O III] $\lambda\lambda 4959, 5007$ emission ($\text{EW}([\text{O III}]\lambda\lambda 4959, 5007) > 100\text{\AA}$, up to $\sim 1000\text{\AA}$). This strong emission is thought to be related to a non zero ionizing photon escape fraction (e.g., Jaskot & Oey 2014; Nakajima & Ouchi 2014). The typical physical properties of GPs are a low stellar mass ($\sim 10^{8.5}M_\odot < M_\star < 10^{10.5}M_\odot$), low metallicity ($12 + \log(\text{O}/\text{H}) = 8.05 \pm 0.14$, Amorín et al. 2010, 2012), high sSFR (sSFR=SFR/stellar mass, 1 to 10 Gyr^{-1} , Cardamone et al. 2009), young age (few Myr), showing Wolf-Rayet signatures (e.g., bumps and He II $\lambda 4686$ emission line), and extremely large H α and [O III] $\lambda 5007$ equivalent widths. Their strong Ly α emission has been recently observed (Henry et al. 2015). However, currently, no direct LyC signatures have been identified in green peas and the work is still ongoing.

Similarly, it would be desirable to find Lyman continuum emitters at even higher redshift, within the first 2 Gyr after the Big-Bang ($z > 3$) and to look for properties and physical mechanisms that allow ionizing photons to escape. Amorín et al. (2014a) report the properties of a $z = 3.417$ galaxy with possible indirect signature of ionizing photon leaking such as a large [O III]/[O II] ratio, but only an upper limit on the Lyman continuum emission. Very recently a class of candidate of strong H β + [O III] emitters has been identified at much higher redshift ($z > 6.5$) by looking at the *Spitzer*/IRAC excess in channels 1 or 2 (depending on redshift; Schaerer & de Barros 2010; Ono et al. 2012; Labbé et al. 2013; Smit et al. 2014, 2015; Roberts-Borsani et al. 2015). The redshift of two of them have been spectroscopically confirmed at $z = 7.73$ and 8.67 with a combined equivalent width $\text{EW}(\text{H}\beta + [\text{O III}]) \simeq 720\text{\AA}$ and $> 1000\text{\AA}$ (rest-frame), respectively (Oesch et al. 2015; Roberts-Borsani et al. 2015; Zitrin et al. 2015).

The nature of these objects is not well understood and further investigation is needed, though this will have to await the James Webb Space Telescope and the Extremely Large Telescopes.

We have identified two Lyman continuum leakers in Vanzella et al. (2015), hereafter V15: *Ion1* and *Ion2*. These galaxies have been selected as Lyman continuum emitters through a photometric selection which is based on the comparison between the observed photometric fluxes and colors probing the Lyman continuum emission and predictions from the combination of spectral synthesis models (e.g., Bruzual & Charlot 2003) and intergalactic medium (IGM) transmissions (Inoue et al. 2014).

In this work we present the source with one of the largest [O III] $\lambda\lambda 4959, 5007$ line equivalent width currently known ($\text{EW} \sim 1500\text{\AA}$, rest-frame) at $z > 3$ and with a plausible leakage of ionizing radiation. Ultraviolet (VLT/VIMOS), optical and NIR (Keck/MOSFIRE) rest-frame spectroscopy are presented, as well as a detailed multi-frequency analysis with the aim to test the aforementioned signatures of linking Lyman continuum. We also use the extreme line ratios to investigate the nebular conditions. To this aim we also compare the observed *Ion2* properties with theoretical predictions from photoionization models.

Ion2 shares some of the properties of sources recently identified at much higher redshift (in particular the large $\text{EW}(\text{H}\beta + [\text{O III}])$ and is therefore relevant to reionization, with the advantage to anticipate the rest-frame optical spectroscopic investigation of such extreme objects.

The paper is structured as follows. The spectroscopic and photometric data are described in Sect. 2. In Sect. 3, we present the physical properties derived from the reanalyzed UV spectrum and the newly acquired NIR MOSFIRE spectrum, and alongside we present the properties derived from the photometry. We also review previously reported properties (V15) in the light of the new data. In Sect. 4, we discuss a possible AGN contribution to the observed *Ion2* spectra. We summarize our main conclusion in Sect. 5.

We adopt a Λ -CDM cosmological model with $H_0 = 70 \text{ km s}^{-1} \text{ Mpc}^{-1}$, $\Omega_m = 0.3$ and $\Omega_\Lambda = 0.7$. We assume a Salpeter IMF (Salpeter 1955). All magnitudes are expressed in the AB system (Oke & Gunn 1983).

2. Data

2.1. Spectroscopy

The available low (LR, $R=180$) and medium (MR, $R=580$) resolution VLT/VIMOS spectroscopy covering the spectral ranges $3400\text{--}7000\text{\AA}$ and $4800\text{--}10000\text{\AA}$ have been obtained during 2005,

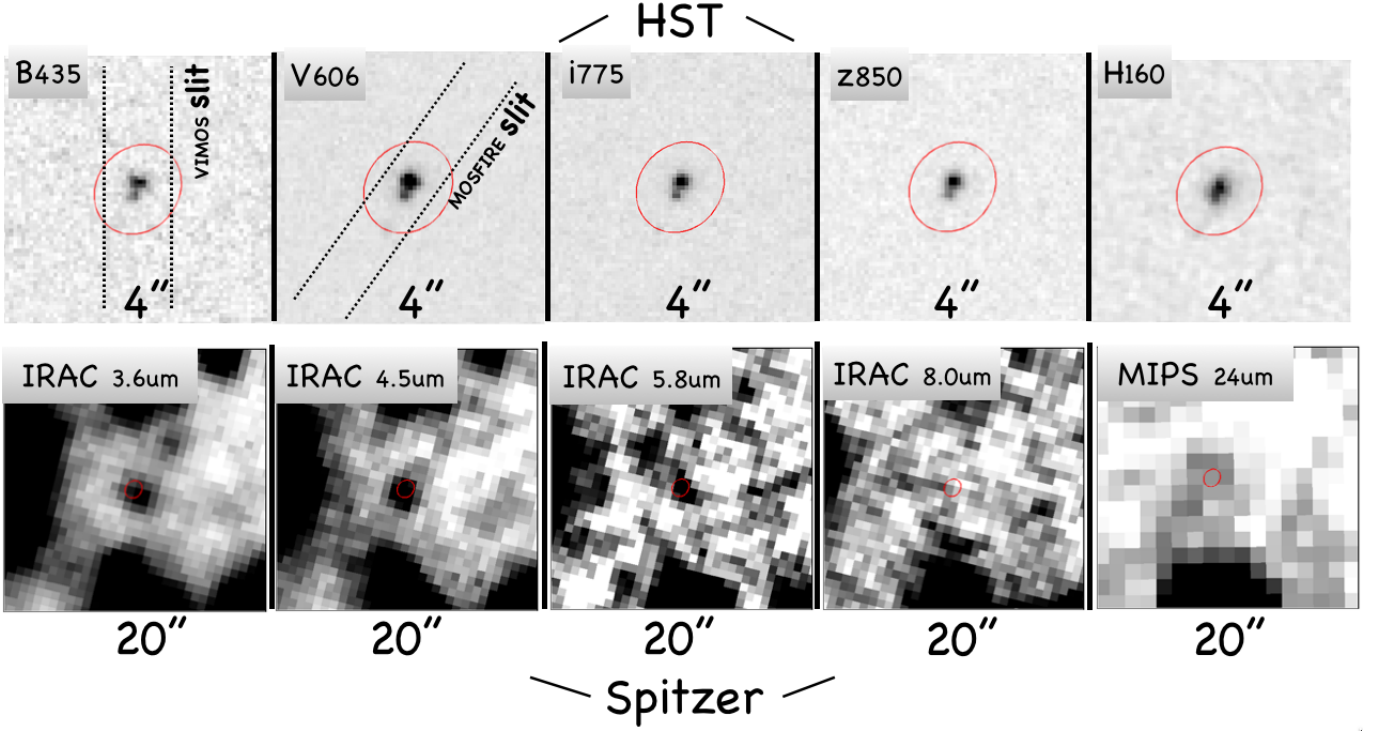


Fig. 1. Postage stamps of *Ion2* in B_{435} , V_{606} , i_{775} , z_{850} , H_{160} , IRAC $3.5\mu\text{m}$, IRAC $4.5\mu\text{m}$, IRAC $5.8\mu\text{m}$, IRAC $8.0\mu\text{m}$ and MIPS $24\mu\text{m}$. The sizes of the images are $4'' \times 4''$ for the *HST* bands and $20'' \times 20''$ for the *Spitzer* bands.

with 4hr exposure time for both LR and MR spectra. The LR spectrum continuum sensitivity is $S/N \sim 0.8$ at 3700\AA with 4 hours and $m(\text{AB}) = 26.5$ assuming seeing $0.8''$ and airmass 1.2. It is calculated over one pixel along dispersion and $2 \times \text{FWHM}$ along spatial direction. (Popesso et al. 2009; Balestra et al. 2010). Slit widths of $1''$ were adopted and the median seeing during observations was $0.8''$. We have newly reduced both configurations, in particular focusing on the Lyman continuum emission (LR-spectrum) and the ultraviolet spectral properties in the non-ionizing domain (MR-spectrum). Reduction has been done as described in Balestra et al. (2010) as well as adopting the AB-BA method described in Vanzella et al. (2011, 2014b). Both methods produce consistent results.

Recently, a near infrared spectrum of *Ion2* has also been obtained with Keck/MOSFIRE during spring 2015 (PI: Günther Hasinger). 32, 32 and 36 minutes integration time have been obtained in the J , H and K bands, respectively, with the AB-BA dithering pattern of $2.9''$. The adopted slit width was $0.7''$ producing a dispersion of 1.30\AA , 1.63\AA , 2.17\AA per pixel, in the J , H and K band, respectively; the pixels scale along the spatial direction was $0.18''/\text{pix}$. *Ion2* was inserted in a mask aimed to target also low- z objects. The J band is useful to monitor low- z emission lines.

Reduction has been performed using the standard pipeline¹. Briefly, two-dimensional sky-subtracted spectra, rectified and wavelength calibrated are produced, from which the one dimensional variance weighted spectrum is extracted with a top-hat aperture. Wavelength solution has been computed from sky emission lines (e.g., Rousselot et al. 2000) in the three bands reaching an RMS accuracy better than $1/20$, $1/30$ and $1/40$ of the pixel size in J , H and K bands, respectively (typical r.m.s. $< 0.05\text{\AA}$).

Flux calibration has been performed by observing the standard star AOV HIP 26577. Given the slit width ($0.7''$) and the median seeing conditions during observations ($0.85''$), particular care must be devoted to slit losses. For this reason we check it by using a star included in the same science mask (WISE 895), for which the continuum is very well detected in the entire MOSFIRE wavelength range, and whose J , H and K band total magnitudes are known from CANDELS (Grogin et al. 2011; Koekemoer et al. 2011) and HUGS photometry (Fontana et al. 2014) with typical $S/N > 40$. From the star WISE 895 and its near infrared photometry we derive a correction factor for slit losses and possible centering effects of about 50%. With this correction the total line flux ($H\beta + [\text{O III}] \lambda\lambda 4959, 5007$) derived from the MOSFIRE spectrum is fully consistent with the total line flux derived from the SED fit and K -band excess (see Section 3.3). *Ion2* is composed by two blobs separated by $0.2''$ (see Figure 1²) each one with a half-light radius $Re \simeq 0.3\text{kpc}$, or less than $0.1''$ at $z = 3.212$. Therefore the slit losses for the entire system at the $0.7''$ MOSFIRE entrance slit are modulated primarily by the seeing during observations, which was on average $0.85''$. A correction factor of 1.4 is consistent with the expected fraction of light falling outside the slit for a perfect centering of the target and Gaussian seeing with $\text{FWHM} = 0.85''$. The correction is also compatible with the discussion in Steidel et al. (2014). Therefore a correction factor of 1.5 is reasonable in our configuration, observational conditions and including a possible small centering uncertainty.

Line fluxes, errors and limits from VIMOS and MOSFIRE spectra are reported in Table 1.

² Created with the Rainbow Navigator tool, https://rainbow.fis.ucm.es/Rainbow_navigator_public/

¹ <https://code.google.com/p/mosfire/>

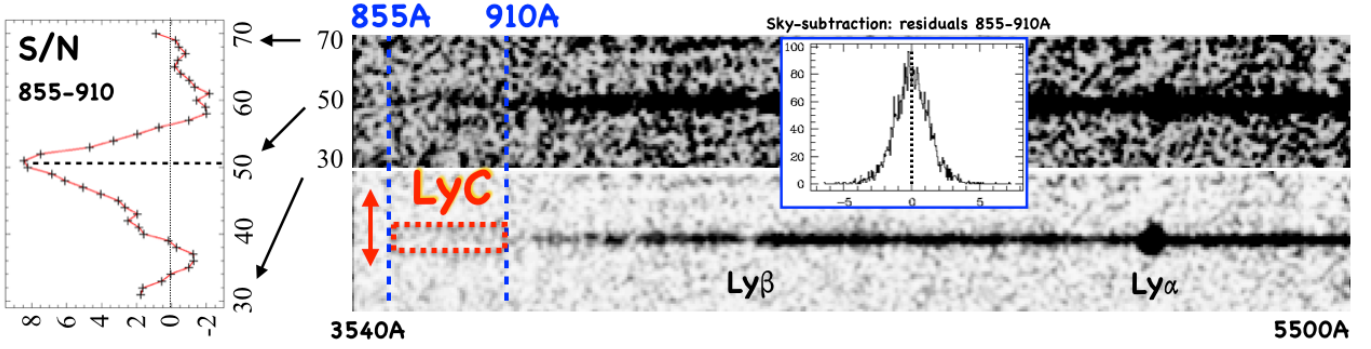


Fig. 2. Two-dimensional LR VIMOS UV spectrum of *Ion2* with different cuts to highlight the spectral features $\text{Ly}\alpha$ and $\text{Ly}\beta$ (bottom) and the Lyman continuum $\lambda < 912\text{\AA}$, in the range 855-910 \AA (top, vertical dotted blue lines). We show the moving average calculated within a rectangular aperture (855-910 $\text{\AA} \times 1.25''$, red-dotted rectangle) in the spatial direction divided by its r.m.s. on the left side. A signal is detected at $\lambda < 912\text{\AA}$ with $S/N > 5$. The inset shows the pixel distribution of the background after sky-subtraction in the region 855-910 \AA (derived from the S/N spectrum). The distribution is symmetric (skewness = -0.016) with the mean and median close to zero, +0.0057 and -0.014, respectively. No significant systematic effects are present.

2.2. Photometry

Deep U band imaging has been taken with the VLT/VIMOS instrument providing a $1-\sigma$ depth of mag ~ 30 within 1 circular aperture. We refer the reader to Nonino et al. (2009) for a complete description of the data reduction (see also Vanzella et al. 2010a).

The photometry from the U VIMOS band to the *Spitzer*/IRAC 8.0 μm band is taken from the CANDELS GOODS-S multi-wavelength catalog (Guo et al. 2013). The optical *Hubble Space Telescope* (*HST*) images from the Advanced Camera for Surveys (ACS) combine the data from Giavalisco et al. (2004), Beckwith et al. (2006) and Koekemoer et al. (2011). The field was observed in the F435W, F606W, F775W, F814W and F850LP bands. Near-infrared WFC3/IR data combines data from Grogin et al. (2011), Koekemoer et al. (2011) and Windhorst et al. (2011), with observations made in the F098M, F125W, and F160W bands. The VLT/HAWK-I K_s band imaging are taken from the HUGS survey (Fontana et al. 2014). The *Spitzer*/IRAC 1 and 2 data are taken from the SCANDALS survey (Ashby et al. 2015), while the IRAC 3 and 4 are taken from Ashby et al. (2013). Hereafter, we will refer to the filters F435W, F606W, F775W, F814W, F850LP, F098M, F125W, F160W as B_{435} , V_{606} , i_{775} , I_{814} , z_{850} , Y_{098} , J_{125} , H_{160} , respectively.

We also check detection in *Spitzer*/MIPS bands and in the *Herschel* data. As shown in Figure 1, we are able to put an upper limit to the MIPS 24 μm flux ($S/N < 2$, $m_{\text{AB}} = 22.27 \pm 0.90$, Santini et al. 2009), while it is undetected in *Herschel* bands ($< 1.2\text{mJy}$, $< 1.2\text{mJy}$, $< 2.4\text{mJy}$ in the 70 μm , 100 μm , and 160 μm bands, respectively, 5σ upper limits).

3. Physical properties

3.1. Spectroscopic detection and spatial distribution of the Lyman continuum emission

Spectroscopic detection of stellar Lyman continuum emission at $z \sim 3$ has been previously claimed for few galaxies (e.g., Steidel et al. 2001; Shapley et al. 2006) but this kind of detection remains a difficult task, mainly because of foreground contamination (Vanzella et al. 2010b; Siana et al. 2015; Mostardi et al. 2015), and a clear spectroscopic detection of Lyman continuum emission at high-redshift is still missing. The only two

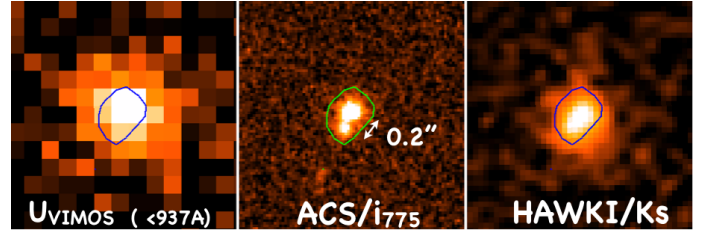


Fig. 3. Ground based VLT/VIMOS U-band observation of *Ion2* at a resolution of 0.2''/pixel (left panel). The contour of the system (derived from the ACS/ i_{775} band, center panel) is indicated and superimposed in blue to the VIMOS U-image and to the HAWK-I K_s image (right panel). The cutouts are 2.6'' vs. 2.6''.

spectroscopic detections reported in literature are from Steidel et al. (2001) in a stack of 29 LBGs and individually in a subsequent spectroscopic follow-up, in 2 out of 14 LBGs observed by Shapley et al. (2006), dubbed D3 and C49. Vanzella et al. (2010b) performed dedicated simulations to derive the probability of foreground contamination, specifically for Steidel et al. (2001) and (Shapley et al. 2006) adopted observational setups. In both cases, the probability was high enough to rise the doubt on their reliability. Subsequently the two sources with possible LyC detection of Shapley et al. (2006) have not been confirmed as LyC sources. In particular D3 was ruled out with much deeper narrow band imaging by Iwata et al. (2009) and Nestor et al. (2011) and C49 was excluded from the list of LyC sources after the possible spectroscopic confirmation of a close foreground lower redshift source (Nestor et al. 2013) and finally confirmed to be a $z=2.029$ foreground source (Siana et al. 2015). Therefore, at present there are not direct LyC detections from star-forming galaxies, apart the source reported in the present work.

The VIMOS LR spectrum of *Ion2* shows a clear signal detected blueward the Lyman limit. We performed a careful re-analysis of the *Ion2* low-resolution UV spectrum by computing the moving average of the flux at $\lambda < 910\text{\AA}$ and we find a signal with $S/N > 5$ (Figure 2). While several systematics can affect the derivation of the LyC signal (e.g., background subtraction Shapley et al. 2006), we use different methods of sky subtraction (ABBA method and polynomial fitting with different orders) and they all provide consistent results. In particular the same moving average in the LyC region calculated over the S/N

Table 1. Emission line properties.

Line	Flux ^a	Dust corrected flux ^b	FWHM ^c	EW ^d	z
Ly α	15.4 ± 1.0^e	$15.4^{+26.0}_{-1.0}$	240 ± 60^f	94 ± 20^e	$3.2183^f \pm 0.003$
Ly α (blue)	5.1	3.2126 ± 0.005
Ly α (red)	10.3	3.2183 ± 0.003
N v λ 1240	< 0.16	< 0.4
C iv λ 1550	< 0.18	< 0.4
He II λ 1640 ^g	0.6 ± 0.3	$0.6^{+1.3}_{-0.2}$
O III λ 1666 ^g	0.5 ± 0.3	$0.5^{+1.2}_{-0.3}$
C III λ 1909	1.3 ± 0.3	$1.3^{+2.3}_{-0.3}$	400 ± 90^h	18^{+9}_{-5}	3.2127
[O II] λ 3727 ⁱ	1.5 ± 1.5	$1.5^{+3.3}_{-1.5}$...	< 50	3.2126
H β ^g	1.5 ± 0.8	$1.5^{+1.5}_{-0.8}$...	112 ± 60	3.2128 ± 0.005
[O III] λ 4959	5.4 ± 0.8 (7.4 ± 1.1)	$7.4^{+4.6}_{-1.1}$	155 ± 70	365 ± 70	3.2128 ± 0.0008
[O III] λ 5007	22.1 ± 0.8	$22.1^{+10.8}_{-0.8}$	147 ± 30	1103 ± 60	3.2126 ± 0.0006

^a Observed emission line flux and error corrected for slit losses (50%) in units of 10^{-17} erg s⁻¹ cm⁻². In parenthesis, the [O III] λ 4959 flux adopting the theoretical ratio [O III] λ 5007/[O III] λ 4959 = 3 (Storey & Zeippen 2000).

^b The emission line dust correction method is described in Appendix A.

^c FWHM (instrumental corrected) and error in units of km s⁻¹.

^d Equivalent width and error in units of Å.

^e Sum of the two components.

^f Main component.

^g Marginal detections (Figure 6): $S/N(\text{O III}\lambda 1666) \sim 1.7$, $S/N(\text{He II}\lambda 1640) \sim 2$, and $S/N(\text{H}\beta) \sim 2$

^h FWHM is the contribution of the two blended components, 1907Å-1909Å.

ⁱ The error is large because the line is on the top of a sky line (Figure 4).

two-dimensional spectrum we derived with ABBA method (see Vanzella et al. 2014a) produces stable results with no significant systematics and a signal ($> 5\sigma$) at the same spatial position of the target. This signal can be interpreted as a direct detection of the Lyman continuum emission, but the presence of the two components in the *HST* images can cast some doubts about the origin of this detection. However, assuming that the faintest component keeps the same magnitude as the derived B_{435} magnitude (27.25 ± 0.24 ; V15) at shorter wavelengths, the average S/N in the range 3600-3840Å is ~ 0.5 per pixel (from ETC). Averaging over 20 pixels, as we did in Figure 2, we would expect $S/N \sim 2.2$. In addition, the B -band dropout signature of such a component ($B-V = 0.62$, V15) between the B_{435} and V_{606} prevents a possible increased emission approaching the U -band, unless an emission feature is boosting the U -band magnitude. In such a case the only possible line would be [O II] λ 3727 which would also imply a certain amount of star-formation activity, that in turns would be detectable through Balmer and/or Oxygen lines in the wide spectral range probed here. The most likely explanation is that the spectroscopic detection is due to a Lyman continuum emission emerging from the brightest *Ion2* component. Furthermore, the ground-based VLT/VIMOS U -band spatial distribution shows that most of the U -band flux is emitted from the brightest component (Figure 3).

However, the U -band probes both ionizing and non-ionizing photons ($\lambda < 937\text{Å}$), so a fraction of the signal is not due only to Lyman continuum photons, and the ground-based observations are clearly limited in terms of resolution, as seen in Figure 3.

The only way to clarify the exact position and the detailed spatial distribution of the Lyman continuum emission is to perform dedicated *HST* observations. A proposal to observe *Ion2* with *HST*/F336W (17 orbits) has been recently approved (PI: Vanzella, cycle 23). Hopefully, emission line diagnostics can be used to characterize the gaseous and stellar content of *Ion2* and provide some hints about a Lyman continuum leakage, as discussed in the next Section.

From the signal detected at 880–910Å, we derive the relative $f_{\text{esc}}(\text{LyC})$ defined as:

$$f_{\text{esc,rel}} = \frac{(L_{\text{UV}}/L_{\text{LyC}})^{\text{intrinsic}}}{(F_{\text{UV}}/F_{\text{LyC}})^{\text{observed}}} \exp(\tau_{\text{LyC}}), \quad (1)$$

where $(L_{\text{UV}}/L_{\text{LyC}})^{\text{intrinsic}}$ is the intrinsic UV to ionizing luminosity density, $(F_{\text{UV}}/F_{\text{LyC}})^{\text{observed}}$ is the observed UV to ionizing flux density, and $\exp(\tau_{\text{LyC}})$ is the LyC attenuation due to the IGM. The signal measured in the LR spectrum corresponds to ~ 26.95 AB magnitude and $m_{1500} = 24.60$ is the magnitude observed at 1500Å rest-frame (using the V_{606} band corrected for the Ly α flux). The average IGM transmission is 0.54 in the 880 – 910Å range (Inoue & Iwata 2008; Inoue et al. 2014) and assuming $L_{1500}/L_{900} = 3$ (Nestor et al. 2013), we get:

$$f_{\text{esc,rel}} = 0.64^{+1.10}_{-0.10} \quad (2)$$

If we relax the assumption about the intrinsic L_{1500}/L_{900} ratio, then $f_{\text{esc,rel}}$ increases. Or conversely, assuming the maximum IGM transmission at $z = 3.2$ (0.74), L_{1500}/L_{900} must be lower than 6.5 to keep $f_{\text{esc,rel}} < 1$.

3.2. Physical properties of the interstellar medium

As described in Section 2, we use VLT/VIMOS and Keck/MOSFIRE spectroscopy to obtain a wide *Ion2* spectral coverage with $850\text{Å} < \lambda < 5700\text{Å}$ (rest-frame). The emission line fluxes, full widths half maximum and equivalent widths are summarized in Table 1. Several lines are barely detected with signal-to-noise < 3 (e.g., H β). However, thanks to the well constrained redshift (see below) and because we know exactly the wavelength position of some features, we do not expect strong systematics. This is the case for the H β and [O II] λ 3727 lines, whose signature are indeed at the expected positions.

Individual line flux errors have been derived using the error spectrum. Additionally, we perform simple simulations to test the error associated to emission lines ratios in the MOSFIRE

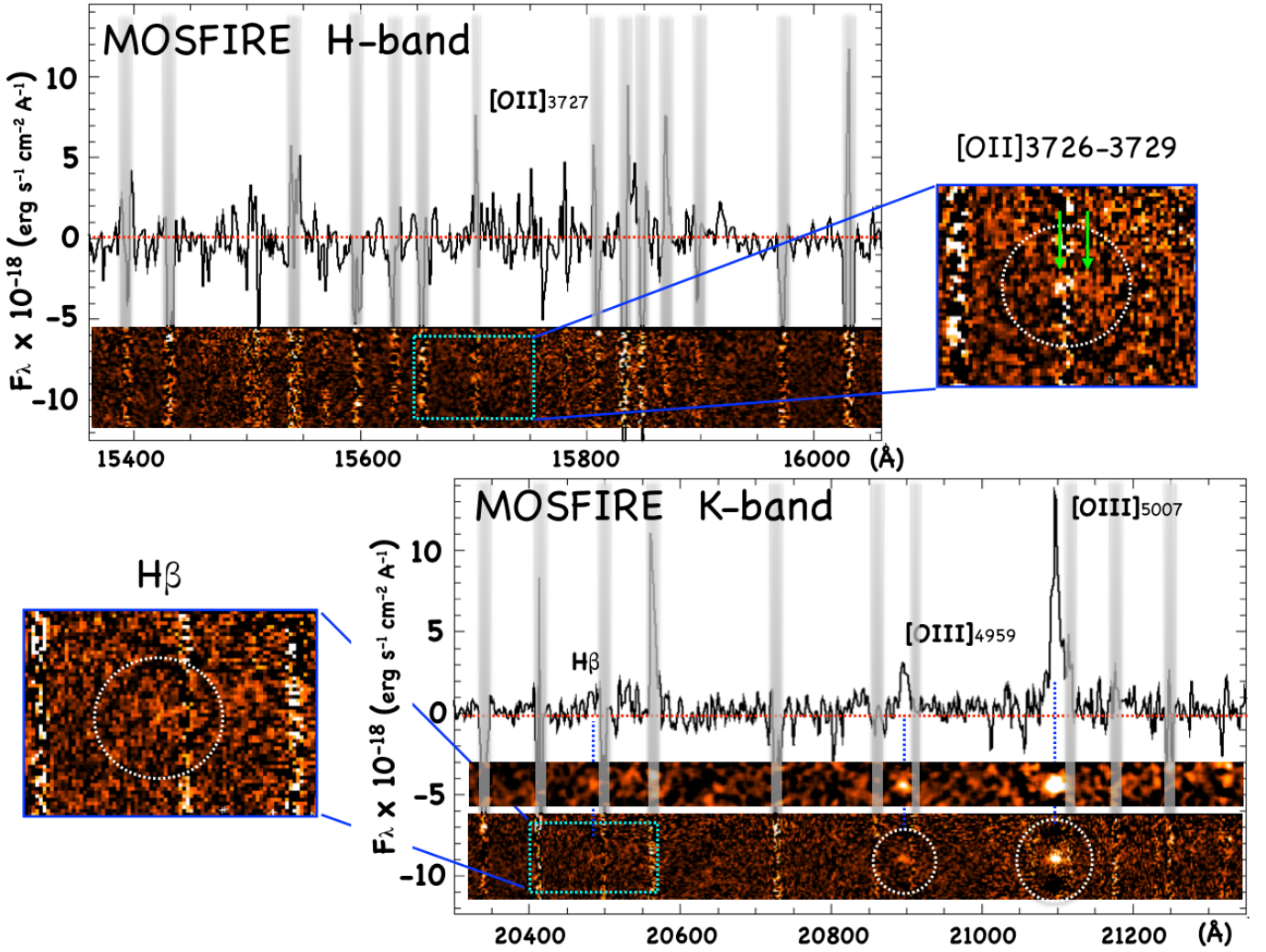


Fig. 4. Two- and one-dimensional NIR spectra of *Ion2* in the MOSFIRE *H* and *K*-band. Two insets show the regions where $H\beta$ and the [O II] $\lambda 3727$ doublet are expected accordingly with the redshift. The gray stripes in the one-dimensional spectra indicate the position of the sky lines.

spectrum (Figure 4). Figure 5 shows the positions where the [O III] $\lambda 5007$ observed line has been added to the sky-subtracted spectrum (marked with numbers from 1 to 10) with different dimming factors (DIM=1, 3, 10, from top to bottom). This provides a rough estimate of the typical error and S/N ratio of our measurements. For example, the typical error associated to the line ratio is [O III] $\lambda 5007$ /[O III] $\lambda 4959 = 4.1 \pm 0.7$, which is consistent with the theoretical ratio (2.99) within 1.4σ (if necessary, we fix the ratio to the theoretical one). Furthermore, the [O III] $\lambda 5007$ line dimmed by a factor 10 (lowest panel in Figure 5) is similar to the observed $H\beta$ 2D spectrum, indicating a likely [O III] $\lambda 5007$ to $H\beta$ ratio ≥ 10 . The marginal $H\beta$ detection (with $S/N \sim 2$) allows us to derive a ratio [O III]/ $H\beta = 14.7 \pm 5.1$, while for the [O II] line the non-detection translates to a 2σ lower limit of [O III] $\lambda 5007$ /[O II] $\lambda 3727 > 10$ (uncorrected for dust in both cases). The errors derived with our simulations are fully consistent with those derived from the error spectrum.

The first property derived from emission lines is the spectroscopic redshift. As already reported in V15, the C III] $\lambda 1906.68 - 1908.68$ transition is clearly detected in the VIMOS MR spectrum (with $S/N = 8$, Figure 6). This feature shows a symmetric shape with a relatively large FWHM ($= 400 \text{ km s}^{-1}$) with respect to other lines like Ly α and [O III], suggesting the two compo-

nents have similar intensities, even if they are blended and non resolved. The redshift we derive from C III] is fully consistent with the redshift of Oxygen lines $4959-5007\text{\AA}$ identified in the MOSFIRE spectrum (see Table 1). This provides a robust estimate of the systemic redshift, $z = 3.2127 \pm 0.0008$.

We derive ionization parameter, Oxygen and Carbon abundances using a modified version of the HII-CHI-mistry code (Pérez-Montero 2014), adapted to provide metallicity, C/O and ionization parameter in a Te-consistent framework, based on the comparison of the observed UV and optical nebular lines with a grid of CLOUDY photoionization models (Ferland et al. 2013). The lines used as input are C IV] $\lambda 1550$, C III] $\lambda 1909$, O III] $\lambda 1666$, $H\beta$, while the C IV] $\lambda 1550$ /C III] $\lambda 1909$ (sensitive to the ionization parameter), C III] $\lambda 1909$ /O III] $\lambda 1666$ (proportional to C/O), [O III] $\lambda 5007$ /O III] $\lambda 1666$ (sensitive to the electron temperature) and (C IV] $\lambda 1550$ +C III] $\lambda 1909$)/ $H\beta$ ratios are compared with model-based ratios in a χ^2 -weighted minimization scheme. The derived abundances and ionization parameter are $12 + \log(\text{O}/\text{H}) = 8.07 \pm 0.44$, $\log(\text{C}/\text{O}) = -0.80 \pm 0.13$, and $\log U = -2.25 \pm 0.81$. We also derive these quantities using all the lines except O III] $\lambda 1666$ ($S/N \sim 1.7$) and we obtain $12 + \log(\text{O}/\text{H}) = 7.79 \pm 0.35$ and $\log U = -2.32 \pm 0.11$ (C/O can not be derived without O III] $\lambda 1666$). Both set of lines lead

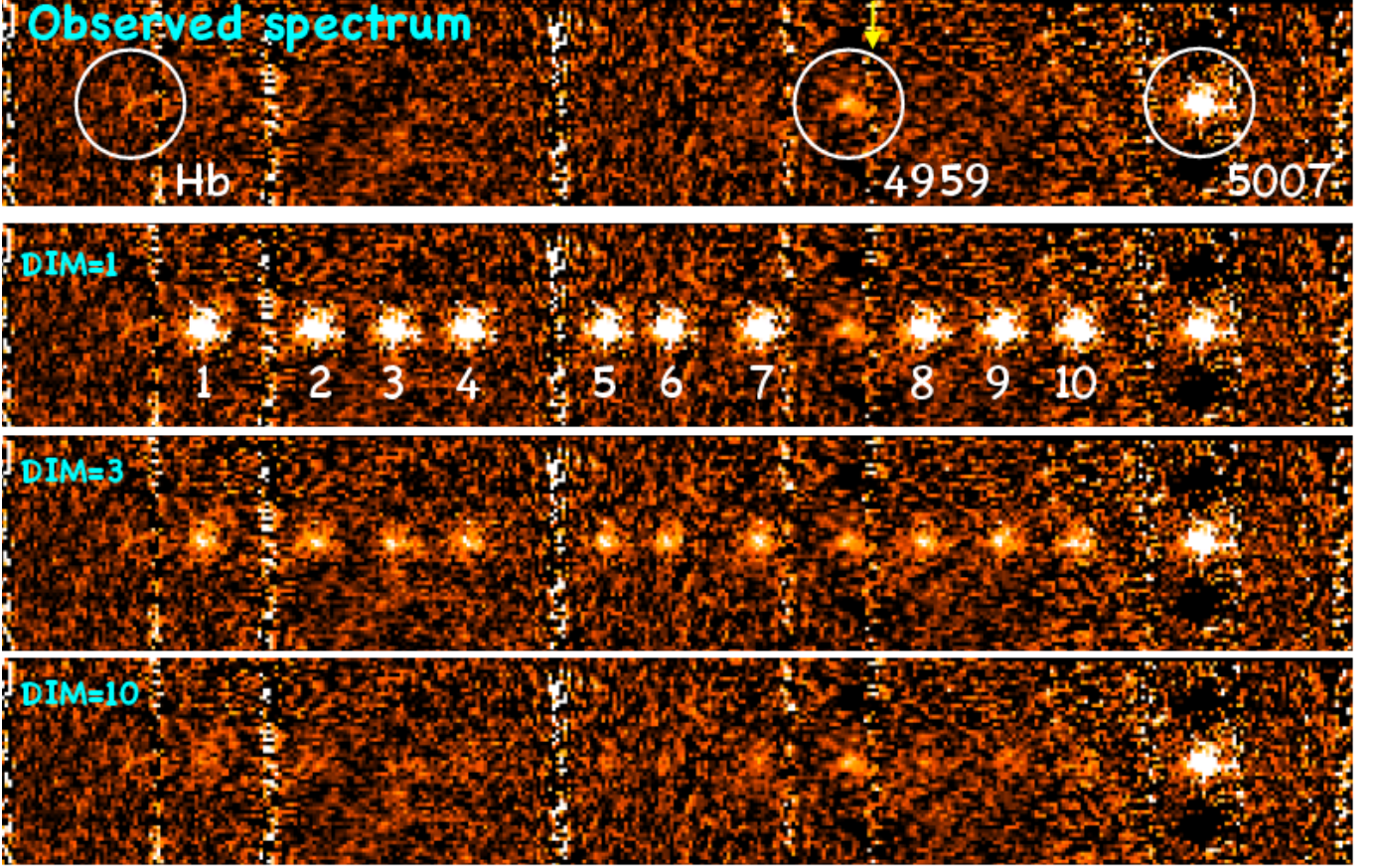


Fig. 5. Observed and simulated two-dimensional MOSFIRE spectrum, with the observed [O III] λ 5007 line replicated at different wavelength positions with different dimming factors (DIM). See text.

to low metallicity and high ionization parameter (in the following, we consider the results obtain with all the line measurements and upper limits). *Ion2* metallicity is similar to the typical green pea metallicity ($12 + \log(\text{O}/\text{H}) = 8.05 \pm 0.14$, Amorín et al. 2010). The metallicity and ionization parameter are also consistent with extreme emission-line galaxies up to $z \sim 3.5$ (Amorín et al. 2014b,a, 2015). The metallicity of *Ion2* is also consistent with the mean metallicity of star-forming galaxies selected through their extreme EW([O III]) (Maseda et al. 2014; Amorín et al. 2015; Ly et al. 2014). Moreover, the *Ion2* C/O ratio is strongly subsolar ($\text{C}/\text{O}_{\odot} = -0.26$ Asplund et al. 2009) and consistent with the trend in C/O vs. O/H for local galaxies (Garnett et al. 1999), which shows a nearly linear increase in C/O with $Z > 0.2Z_{\odot}$. The low O/H and C/O abundances of *Ion2* are similar to those found in other strong emission-line galaxies at $z \sim 1 - 3$ (e.g., Christensen et al. 2012; Stark et al. 2014; James et al. 2014) and suggest a significant contribution of O and C produced by massive stars, which is also consistent with very young and extreme starbursts.

We compare the metallicity and the ionization parameter with the results presented in Nakajima & Ouchi (2014) in Figure 7. Overall, *Ion2* has a lower metallicity than all other galaxy populations presented in their work and one of the highest ionization parameter. The higher ionization parameter is in

line with a possible Lyman continuum leaking that could be explained with a low neutral hydrogen column density. Also, the *Ion2* extreme [O III] λ 5007/[O II] ratio, the metallicity, and the ionization parameter are consistent with cloudy models with a non zero Lyman continuum escape fraction (Nakajima & Ouchi 2014, , Figure 11)

The identification of Lyman continuum leakage from Green pea galaxies is a current line of research (e.g., Jaskot & Oey 2014; Nakajima & Ouchi 2014; Borthakur et al. 2014; Yang et al. 2015) and the Green pea nature of *Ion2* and its LyC leakage represent the first concrete attempt to link these two properties. *Ion2* represents an extreme case of Green pea galaxy, being the highest redshift ($z > 3$) ultra-strong Oxygen emitter (with $\text{EW}([\text{O III}]\lambda\lambda 4959, 5007) \sim 1100\text{\AA}$) currently known. The Lyman continuum leakage observed in *Ion2* allow us to investigate the relationship between the LyC leakage and physical and morphological properties. However, as shown in Stasińska et al. (2015), the [O III]/[O II] ratio is also related to the specific star formation rate and the metallicity: the [O III]/[O II] ratio increases with increasing sSFR and decreasing metallicity. For *Ion2* the observed ratio is ≥ 15 making *Ion2* as an outlier in the Oxygen abundance vs. [O III]/[O II] ratio relation and the EW(H β) (i.e., sSFR) vs. [O III]/[O II] ratio (Figure 2, Stasińska et al. 2015); *Ion2* ratio is higher by ~ 0.6 dex for the observed

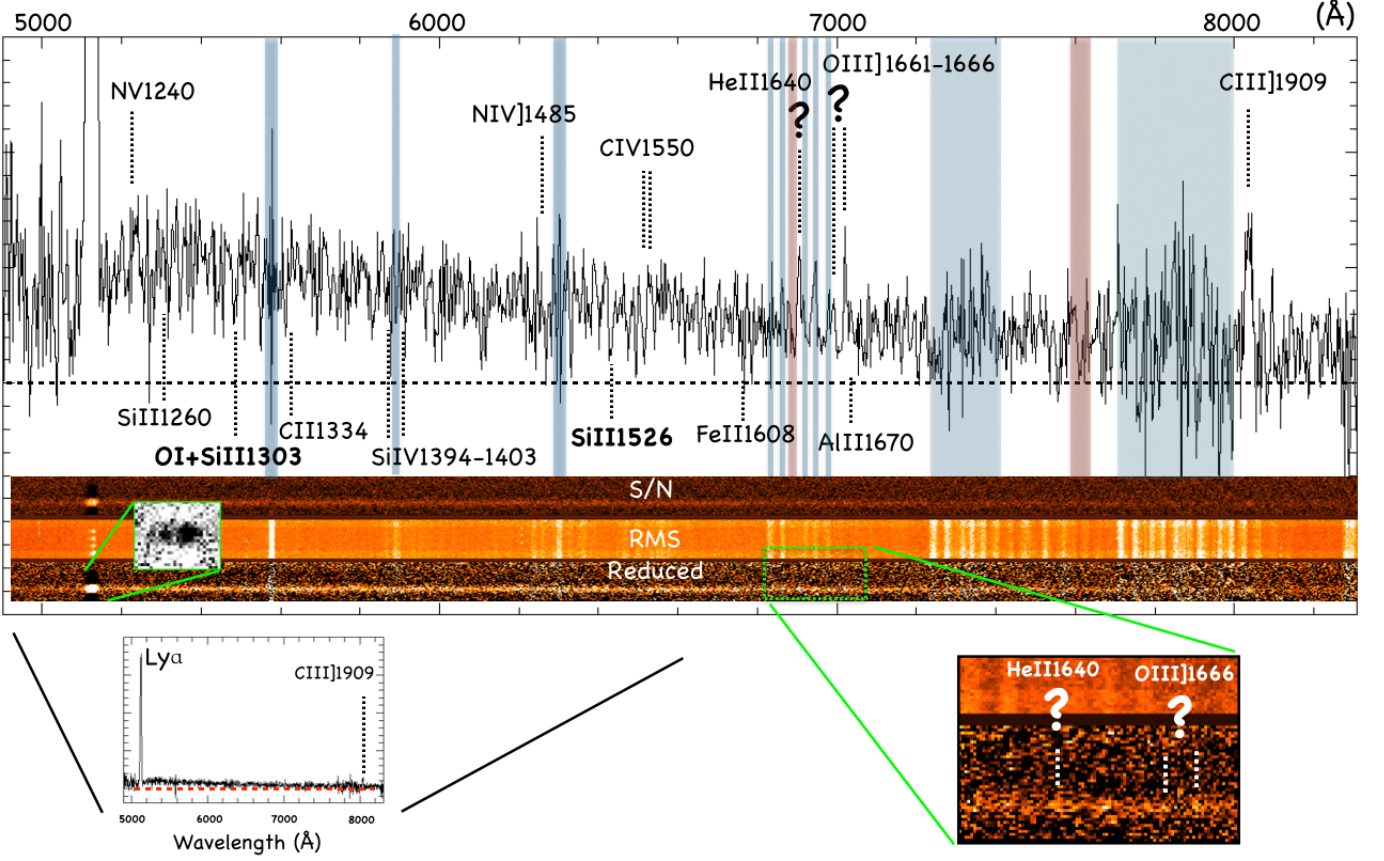


Fig. 6. 1D and 2D UV VLT/VIMOS MR spectra. The transparent blue stripes indicate position of the emission sky lines. The transparent red stripes indicate the telluric molecular sky absorptions bands, *B* and *A* bands at $\sim 6900\text{\AA}$ and $\sim 7600\text{\AA}$. In the same panel, three two-dimensional spectra are shown, the reduced, r.m.s. and signal to noise, from bottom to top, respectively. The inset on the left side shows the double peaked Ly α line (from V15). In the bottom-right a zoom in around He II $\lambda 1640$ and O III $\lambda 1666$ positions is shown. Their detection remain tentative. In the bottom-left, the 1D spectrum is shown allowing to see the relative Ly α flux in comparison with other lines.

EW($H\beta$) (Table 1) and the ratio is higher by ~ 1 dex compared to galaxies in the SDSS sample with similar metallicities. The $Ion2$ [O III]/[O II] ratio is also higher than what is expected for the derived stellar mass, SFR, and sSFR (Nakajima & Ouchi 2014). Therefore, we conclude that the extreme [O III]/[O II] ratio is due to unusual physical conditions (density-bounded nebula), which imply a low column density of neutral gas, and so favor leakage of ionizing photons (Nakajima & Ouchi 2014).

3.3. Physical properties derived from the photometry

While the emission lines highlight *Ion2* ISM physical properties, we also use the photometry to confirm findings such as the large [O III] emission and derive other physical parameters. From Figure 8, the jump in the K-band is evident, $K = 22.97 \pm 0.02$ while the continuum level in the adjacent bands, H_{160} and IRAC Channel 1 is ≈ 24.15 . The $\Delta m \approx 1.1$ magnitude in the HAWKI K-band corresponds to an additional flux of 3.1×10^{-16} erg/s/cm 2 , that corresponds to an observed equivalent width of 6700\AA (1600\AA rest-frame). The total flux derived for $H\beta + [O III] \lambda\lambda 4959, 5007$ from the MOSFIRE spectrum (see Tab. 1) is fully compatible with the flux estimated from the K-band excess (after correcting for slit losses of the three lines, see above). The derived $H\beta + [O III]$ equivalent width is one of the largest ever observed at $z > 2$. The measured line ratios among

the $H\beta + [O III] \lambda\lambda 4959, 5007$ suggest the [O III] $\lambda 5007$ rest-frame equivalent width is $\approx 1100\text{\AA}$, with a similar value to the few extreme cases reported in literature at $z \sim 1 - 2$ (Atek et al. 2011; Amorín et al. 2014b; Maseda et al. 2014). The [O III]/ $H\beta$ ratio is also higher than the one reported in Holden et al. (2014) for LBGs at $z \sim 3.5$, while the ratio is higher in this sample than in the local Universe (Brinchmann et al. 2004). Also at $z > 6$ large equivalent widths of $H\beta + [O III]$ have been reported, measured through photometric excess detected in the Spitzer/IRAC channels (e.g. Finkelstein et al. 2013; Smit et al. 2014; Oesch et al. 2015). While these cases can be spectroscopically investigated only with future facilities, like the *James Webb Space Telescope* (JWST) and Extremely Large Telescope class, in our case the MOSFIRE near infrared spectroscopy has allowed us to access the details of the lines.

We derive the SFR from the UV luminosity, $H\beta$ and Ly α lines (Kennicutt 1998), neglecting dust attenuation (see Appendix B). We get $SFR(UV) = 15.6 \pm 1.5 M_{\odot} \text{ yr}^{-1}$, $SFR(H\beta) = 40.0^{+7.5}_{-25.6} M_{\odot} \text{ yr}^{-1}$, and $SFR(Ly\alpha) = 14.3 \pm 1.0 M_{\odot} \text{ yr}^{-1}$. The three SFR indicators are consistent within 68% confidence levels, while $SFR(H\beta)$ is higher than the two others. The resonant nature of Ly α photons prevents us from deriving precisely the SFR with this line (e.g., Atek et al. 2014). On the other hand, the $H\beta$ line is barely detected (Table 1). The higher SFR derived from the $H\beta$ line can be explained if the

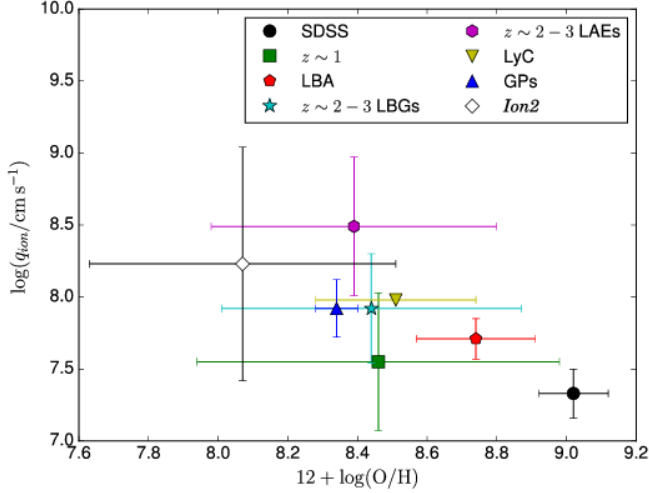


Fig. 7. Comparison of the metallicity and ionization parameter ($U = q/c$) between the mean sample properties from Nakajima & Ouchi (2014) and *Ion2* with 1σ uncertainties. *Ion2* is compared to local galaxies from the SDSS survey, a galaxy sample at $z \sim 1$, a Lyman break galaxy (LBG) sample at $z \sim 2.5$, a Lyman alpha emitter (LAE) sample at $z \sim 2.5$, local Lyman break analogues (LBAs), LyC emitters, and Green Peas (GPs). See Nakajima & Ouchi (2014) and references therein for a complete description of these samples.

age of the galaxy is significantly younger than 100 Myr because of the different equilibrium timescales between UV and nebular emission lines. However, this is not the case according to the SED fitting, with an age for *Ion2* ~ 200 Myr. By comparing SFR(UV) and SFR($\text{Ly}\alpha$), we derive a Lyman- α escape fraction $f_{\text{esc}}(\text{Ly}\alpha) \geq 0.78$ ($f_{\text{esc}}(\text{Ly}\alpha) \geq 0.28$ by using SFR($\text{H}\beta$) instead of SFR(UV)). This high $\text{Ly}\alpha$ escape fraction can be related to a blue β slope (e.g., Hayes et al. 2014), but also to a low H I column density ($N_{\text{H I}} \leq 10^{18} \text{ cm}^{-2}$; Yang et al. 2015; Henry et al. 2015).

Ion2 $\text{Ly}\alpha$ profile has been described in V15: it exhibits a blue asymmetric tail. A low column density would be consistent with the bluer $\text{Ly}\alpha$ emission at the systemic redshift, and also with the high ionization parameter, and so with a leakage of ionizing photons. The star formation activity confined in a small physical volume can also favor the escape of ionizing radiation (e.g., Heckman et al. 2011; Borthakur et al. 2014). Furthermore, detailed analysis of the local blue compact dwarf galaxy NGC 1705 shows that O stars are able to photoionize volumes far from their location (Annibali et al. 2015), which could create density-bounded conditions. Moreover, the spatial density of O stars in NGC 1705 increases toward the center of the galaxy, forming a sort of super star cluster efficient in ionizing its environment. *Ion2* could resemble a similar condition, being spatially resolved, but nucleated in the ultraviolet (1400 Å), in which a young super star cluster could be present in the core and significantly contributing (or totally contributing if the AGN is absent) to the ionization field. Interestingly, because *Ion2* has two components likely at a similar redshift (Section 3.4), the leakage of ionizing photons can also be favored by the merging/interaction of these two components (Rauch et al. 2011).

From SED fitting, we also derive a stellar mass $\log(M_{\star}/M_{\odot}) = 9.5 \pm 0.2$ and an age of the stellar population (since the onset of the star formation) $\log(\text{Age}/\text{yr}) = 8.6 \pm 0.2$.

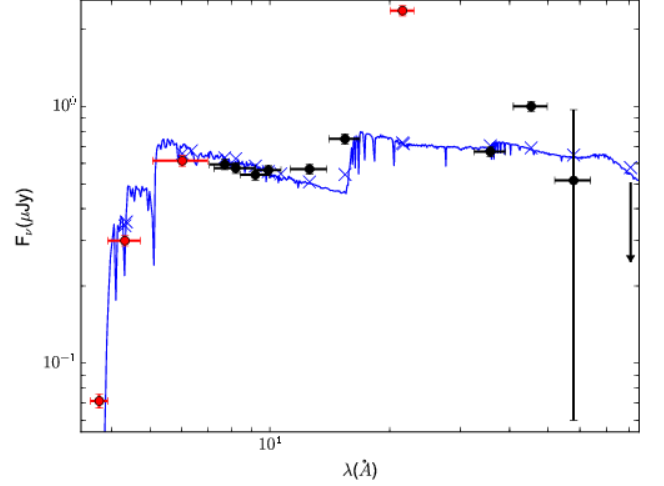


Fig. 8. Observed *Ion2* SED (black and red dots). We show the best SED fit in blue and the integrated fluxes with blue crosses. We exclude photometric points (in red) affected by the IGM and strong emission lines ($\text{Ly}\alpha$, [O III]) from the SED fitting. The arrow indicates 1σ upper limit.

We notice that while the two *Ion2* components are separated in the *BViz* bands, they are seen as a unique galaxy in the other bands, and the stellar mass is the total stellar mass of the two components. Given the very close separation among the two ($0.2''$), we decided to avoid any tentative decomposition and SED fitting of each component individually, especially in the Spitzer/IRAC bands where the pixel size is $1.22''$ and the decomposition is in practice not possible. Using SED fitting and anchoring the best fit to the β slope derived from UV spectrum fitting (Appendix B), we predict the expected observed $\text{L}(\text{IR})_{24\mu\text{m}}$ assuming energy balance (i.e., we assume a balance between the energy absorbed in the UV/optical (we integrate over 912Å to $3\mu\text{m}$) and re-radiated in the IR). The MIPS $24\mu\text{m}$ observations probe the PAH feature at $6.2\mu\text{m}$ (rest-frame) which can be used to derive the total IR luminosity (i.e., IR luminosity integrated over $8\text{--}1000\mu\text{m}$) and then the bolometric SFR (Pope et al. 2008; Rujopakarn et al. 2012). Because the SFR derivation relies on several assumption (star formation history, age, metallicity, IMF, Kennicutt 1998), we rely on the comparison between predicted $\text{L}(\text{IR})_{\text{SED}}$ and derived $\text{L}(\text{IR})_{24\mu\text{m}}$, rather than relying on a SFR comparison. From the MIPS $24\mu\text{m}$ upper limit, we derive $\log(\text{L}(\text{IR})/\text{L}_{\odot})_{24\mu\text{m}} = 9.92^{+0.65}_{-0.44}$, while from SED fitting we derive $\log(\text{L}(\text{IR})/\text{L}_{\odot})_{\text{SED}} = 9.77^{+1.00}_{-2.03}$. The SED predicted and observed $\text{L}(\text{IR})$ are consistent but the uncertainties are too large to exclude an AGN contribution to the IR flux. We further discuss a possible AGN contribution in Section 4.

Ion2 also shows an excess in the IRAC2 band, in comparison with the IRAC1 channel. This excess can not be explained by emission line or other feature from both blobs (e.g., a contamination by a strong emission line as $\text{H}\alpha$ would imply $z > 5.0$ for the emitting galaxy). While we do not have a satisfactory explanation, we note that the rest-frame wavelength interval probed by IRAC2 ($9500\text{Å--}11900\text{Å}$) cannot be explored in detail before the launch of *JWST*. Therefore that part of the spectrum is poorly known, especially for sources in the distant universe. In this work we do not comment further about this feature that,

however, do not affect our results. We summarize the physical properties of *Ion2* in Table 2.

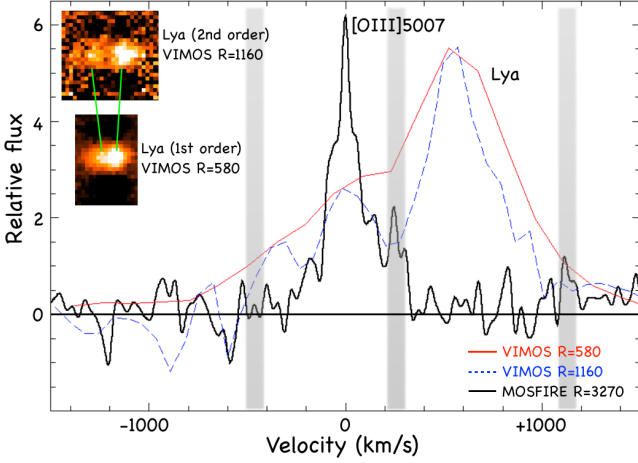


Fig. 9. The velocity profiles of [O III]λ5007 and Lyα lines relative to systemic. [O III]λ5007 line is shown in black, the Lyα first order in red, and the Lyα second order with the dashed blue line. The positions and width of the sky lines are marked with gray stripes.

Table 2. *Ion2* physical properties.

$\log(M_*/M_\odot)$	9.2 ± 0.2
$\log(\text{age}/\text{yr})$	8.6 ± 0.2
$\text{SFR} (M_\odot \text{ yr}^{-1})$	15.6 ± 1.5
$E(B - V)_{\text{stars}}$	≤ 0.04
$12 + \log(\text{O}/\text{H})$	8.07 ± 0.44
$\log q$	8.23 ± 0.81
$\log(\text{C}/\text{O})$	-0.80 ± 0.13

3.4. Properties previously reported: summary

Ion2 has been previously reported as a Lyman continuum emitter candidate in V15. Here, we briefly summarize the *Ion2* properties reported in this latter reference.

Ion2 is a compact source (300 ± 70 parsecs) with two visible components. The presence of these two blobs can be misleading when trying to assess the detection of a possible Lyman continuum emission, because multiple components are often source of foreground contamination (Vanzella et al. 2010b; Siana et al. 2015; Mostardi et al. 2015). However, *BViz* magnitudes have been derived for each component after subtracting the close companion with a GALFIT fitting procedure (see V15). The two show the same break between the V_{606} and B_{435} bands and the absence of any spurious (low- z) emission line along the wide wavelength range probed here (from 3400\AA up to 24000\AA) support that the faint component is a physical companion of the brightest one (i.e., at $z = 3.2$). Furthermore, the slit orientation in the MOSFIRE observation is also maximizing the separation in the spatial direction (see Figure 1), though seeing FWHM is significantly larger than the separation. Therefore from photometric shape and spectroscopic arguments we conclude that the two components are at the same redshift.

Interestingly, the Lyα profile exhibits a double peaked emission, with the bluer component being half of the main red peak and having a redshift consistent with the systemic redshift ($z = 3.212$, Figure 9). If the two Lyα components are due to the two *Ion2* blobs, we would expect multiple-peaked [O III] emissions (Kulas et al. 2012), which are not present in the *Ion2* MOSFIRE spectrum (see Section 3.2). If the observed Lyα photons arise only from the brightest *Ion2* component, as discussed above it can be consistent with a low neutral gas column density (e.g., Verhamme et al. 2015), and with the escape of Lyman continuum photons (Behrens et al. 2014). However, a small shift of the maximum of the profile compare to the systemic redshift is expected in case of Lyman continuum emission (i.e., $\log(N_{\text{H I}}) < 18$), with a maximum peak separation $< 300 \text{ km s}^{-1}$ (Verhamme et al. 2015). But the non detection of low-ionization absorption lines (e.g., [C II]λ1334, [Si II]λ1260) is consistent with a low neutral hydrogen column density allowing the escape of ionizing photons and a low covering fraction along the line of sight (Heckman et al. 2011; Jones et al. 2012, 2013). We possibly detect O I + [Si II]λ1303 with $\text{EW} = -1.2 \pm 0.7\text{\AA}$ and tentatively [Si II]λ1526 with $\text{EW} = -1.0 \pm 0.7\text{\AA}$. However, the signal-to-noise ratio is low ($S/N \sim 2$). Assuming a 1σ fluctuation, we can put a lower limit on the EW of non detected lines as $\text{EW} > -0.7\text{\AA}$. This is in line with the results from Shapley et al. (2003) at $z \sim 3$: galaxies with high Lyα equivalent width exhibit much weaker low-ionization absorption lines than galaxies with low EW(Lyα).

Finally, *Ion2* is not detected in the 6Ms X-ray Chandra image ($L_X < 2 - 3 \times 10^{42} \text{ erg s}^{-1}$) and most of the high-ionization emission lines are not detected (e.g., N Vλ1240, C IVλ1550). However, from the UV spectrum reanalysis, we report a tentative detection of He IIλ1640 (see Sect. 3.2): this line is barely detected in the ABBA spectrum, but not in the Balestra et al. (2010) spectrum. Furthermore, V15 also reported a possible variability of *Ion2*. We further discuss the possibility of an AGN contribution in Section 4.

4. Is *Ion2* an AGN?

We now discuss the possibility that the main source of UV ionizing photons is an AGN. First of all, the UV emission is resolved so it is most probably due to the stellar population, not an AGN. Therefore, an AGN could contribute to the SED but it would not dominate it at all wavelengths.

Unfortunately, we can not use the BPT diagram (Baldwin et al. 1981) to discriminate between star-formation and AGN, because Hα and [N II] emission lines are out of the MOSFIRE wavelength range. Juneau et al. (2011) proposed an alternative to the BPT diagram, with the so-called MEx diagram based on the comparison between stellar mass and [O III]λ5007/Hβ ratio. The probability for an object to be an AGN associated with the MEx diagram is not defined at the *Ion2* position (Juneau et al. 2014), although the large [O III]λ5007 to Hβ ratio would classify *Ion2* as an AGN. Other diagnostic diagrams have been proposed, like the [O III]λ5007/Hβ vs. [O II]λ3727/Hβ (Lamareille et al. 2004). Also in this diagram, *Ion2* would be classified as an AGN, because of the large [O III]λ5007/Hβ ratio. However, for both diagnostics (MEx and [O III]λ5007/Hβ vs. [O II]λ3727/Hβ), there is no known AGN at a similar locus as *Ion2*. Alternatively, photoionization models predict a possible increase of the [O III]/[O II] with decreasing metallicity and increasing ionization parameter (Nakajima & Ouchi 2014).

As already stated, *Ion2* remains undetected even in the 6Ms X-ray Chandra survey. According to the empirical relation between the [O III] $\lambda 5007$ luminosity and the X-ray luminosity (e.g., Panessa et al. 2006), given the extreme [O III] $\lambda 5007$ emission the expected X-ray luminosity would be $L_X \sim 10^{45} \text{ erg s}^{-1}$ if the [O III] $\lambda 5007$ emission is associated to an AGN. Considering the scatter in the $L([\text{O III}]\lambda 5007)$ - L_X relation, we can derive a lower limit of $L_X \geq 5 \times 10^{43} \text{ erg s}^{-1}$ which would be easily detectable in the 6Ms Chandra data (with typical $S/N > 10$), independently on the source position in the X-ray image. However, extremely obscured AGN can have lower X-ray luminosity than expected from the $L([\text{O III}]\lambda 5007)$ - L_X relation, this AGN possibly being Compton-thick AGN (e.g., Vignali et al. 2010). The infrared and X-ray luminosities derived from the MIPS detection and the 6Ms upper limit, respectively, can be compared with the properties of known obscured AGN (Lanzuisi et al. 2015): *Ion2* properties can be only consistent with a faint and highly obscured AGN (e.g., Lutz et al. 2004).

The large EW([O III] $\lambda 5007$) is unusually large for all types of AGN (Table 1, Caccianiga & Severgnini 2011), while such large equivalent width has been already reported for some star-forming galaxies at lower redshift (e.g., Atek et al. 2011; van der Wel et al. 2011; Brammer et al. 2012).

The UV spectrum is quite unexplored as a diagnostic for AGN/star-forming galaxies classification, but the observed narrow lines (Table 1) exclude the presence of broad-line AGN. We also compare *Ion2* emission line ratios with typical UV emission line ratios in narrow line AGN. Nagao et al. (2006) present the UV spectrum analysis of narrow-line QSOs and narrow-line radio galaxies at $1.2 \leq z \leq 3.8$ (see also De Breuck et al. 2000). The first evidence against a possible AGN contribution to *Ion2* spectra is the lack of C IV $\lambda 1550$ detection. This line is detected in all AGN types studied in Nagao et al. (2006). The typical line ratio C III $\lambda 1909$ /C IV $\lambda 1550$ is ~ 0.5 and C IV $\lambda 1550$ /He II $\lambda 1640 \geq 1$, while we measure > 10 and < 1 for *Ion2* respectively. Narrow-line AGN UV spectra at $z \sim 2 - 3$ exhibit a C III $\lambda 1909$ /C IV $\lambda 1550$ ratio near 1 which is also much lower than the *Ion2* ratio (Hainline et al. 2011). The C IV $\lambda 1550$ /C III $\lambda 1909$ ratio can be used to determine the nature of the ionizing source, with C IV $\lambda 1550$ /C III $\lambda 1909 \sim 2$ if the ionizing photons are produced by an AGN and C IV $\lambda 1550$ /C III $\lambda 1909 \sim 0.001$ if population I stars are the ionizing sources (Binette et al. 2003). The clear C III $\lambda 1909$ detection and the C IV $\lambda 1550$ non detection are consistent with a main ionizing source being stars rather than an AGN.

The origin of He II $\lambda 1640$ emission in galaxies has been matter of investigation, possibly produced by massive stars both in the local Universe (e.g., Szécsi et al. 2015; Gräfener & Vink 2015) and at high-redshift (e.g., Cassata et al. 2013; Sobral et al. 2015; Pallottini et al. 2015). He II $\lambda 1640$ detection is generally associated with AGN activity, but it has also been reported that He II $\lambda 1640$ associated with no C IV $\lambda 1550$ is a possible feature in star-forming galaxies at $z \sim 3$ (Cassata et al. 2013). This could be explained by a contribution from population III stars (Sobral et al. 2015). However, as stated in the previous section, we remind that the He II $\lambda 1640$ detection is tentative.

Summarizing, *Ion2* is not detected in the 6Ms Chandra survey and has no broad lines. The extreme [O III]/H β ratio would lead to consider it as an AGN (Lamareille et al. 2004; Juneau et al. 2014), but this ratio can also be explained by extreme ISM physical conditions (Jaskot & Oey 2013; Nakajima & Ouchi 2014). The lack of X-ray detection can be explained with an obscured AGN (Vignali et al. 2010), but the lack of C IV $\lambda 1550$

detection in the UV spectrum is likely inconsistent with this hypothesis. Therefore, the main argument against an AGN contribution is the lack of the C IV $\lambda 1550$ emission line. If an AGN contributes to the *Ion2* emission, it is likely a faint and obscured AGN with peculiar photoionization conditions (De Breuck et al. 2000).

5. Conclusions

In this paper, we present new observations with the Keck/MOSFIRE NIR spectrograph and a new analysis of the UV spectrum of a Lyman continuum emitter candidate. *Ion2* is an object at $z = 3.212$ composed of two distinct blobs, nucleated and resolved in the rest-frame UV, indicating emission from star-forming regions. *Ion2* is also a candidate Lyman continuum emitter with U band flux consistent with a leakage of ionizing photon ($P(f_{\text{esc}}(\text{LyC}) = 0) < 10^{-4}$), as reported in V15. Contamination from foreground galaxies can be ruled out.

Our main results can be summarized as follows:

- a new analysis of the UV spectrum shows a signal consistent with a direct detection of ionizing photons with $S/N > 5$ and a relative Lyman continuum escape fraction $f_{\text{esc,rel}} = 0.64^{+1.10}_{-0.10}$,
- the Ly α emission at the systemic redshift, the high Ly α escape fraction, the non detection of low-ionization absorption lines are consistent with a low neutral hydrogen column density, while velocity separation of the two Ly α peaks is in tension with expectation (e.g., Verhamme et al. 2015);
- we find low metallicity ($\sim 1/6Z_{\odot}$), strongly subsolar C/O ratio and high ionization parameter ($\log U = -2.25$) using a T_e -consistent method, in good agreement with previous results at $z \sim 2 - 3$;
- *Ion2* exhibit one of the largest [O III]/[O II] ratio observed at $z > 3$ and similar large ratios are predicted for galaxies with low metallicities and Lyman continuum leakage (Nakajima & Ouchi 2014);
- there is no clear evidence of AGN contribution to *Ion2* emission;
- the *Ion2* physical properties (SFR, stellar mass, dust attenuation, strong emission lines) are similar to green peas, and the *Ion2* large EW(H β + [O III] $\lambda\lambda 4959, 5007$) is similar with the ones derived for LBGs at $z > 7$.

Ion2 physical properties, morphology, and very strong emission lines make it a possible analog of $z \sim 8$ LBGs. Furthermore, unlike local analogs (e.g., Heckman et al. 2011), *Ion2* probes Lyman continuum emitter properties only ~ 1.5 Gyr after the reionization epoch. From the very large EW([O III] $\lambda\lambda 4959, 5007$ +H β) observed at high-redshift (Oesch et al. 2015; Zitrin et al. 2015; Roberts-Borsani et al. 2015; Smit et al. 2015), we can speculate that these galaxies have a leakage of ionizing photons.

The direct detection of Lyman continuum emission leave little doubt about the fact that *Ion2* emits ionizing flux. This galaxy certainly exhibits peculiar properties which however do not allow to fully discriminate among different possible sources of ionizing radiation yet: stellar emission, faint and obscured AGN, or other ionizing sources. Only high resolution *HST* observations of the ionizing radiation may provide useful clues. In the near future, our approved proposal to observe *Ion2* with *HST*/F336W will hopefully shed new light on the nature of this source (PI: Vanzella).

Acknowledgements. We thank the referee for suggestions for clarifying the text and the analysis. We thank M. Tosi, F. Annibali, M. Brusa and H. Atek for useful

discussions. We acknowledge the financial contribution from PRIN-INAF 2012. This work has made use of the Rainbow Cosmological Surveys Database, which is operated by the Universidad Complutense de Madrid (UCM), partnered with the University of California Observatories at Santa Cruz (UCO/Lick, UCSC).

References

- Amorín, R., Grazian, A., Castellano, M., et al. 2014a, *ApJ*, 788, L4
 Amorín, R., Pérez-Montero, E., Contini, T., et al. 2015, *A&A*, 578, A105
 Amorín, R., Pérez-Montero, E., Vílchez, J. M., & Papaderos, P. 2012, *ApJ*, 749, 185
 Amorín, R., Sommariva, V., Castellano, M., et al. 2014b, *A&A*, 568, L8
 Amorín, R. O., Pérez-Montero, E., & Vílchez, J. M. 2010, *ApJ*, 715, L128
 Annibali, F., Tosi, M., Pasquali, A., et al. 2015, *ArXiv e-prints*
 Ashby, M. L. N., Willner, S. P., Fazio, G. G., et al. 2015, *ApJS*, 218, 33
 Ashby, M. L. N., Willner, S. P., Fazio, G. G., et al. 2013, *ApJ*, 769, 80
 Asplund, M., Grevesse, N., Sauval, A. J., & Scott, P. 2009, *ARA&A*, 47, 481
 Atek, H., Kunth, D., Schaerer, D., et al. 2014, *A&A*, 561, A89
 Atek, H., Siana, B., Scarlata, C., et al. 2011, *ApJ*, 743, 121
 Baldwin, J. A., Phillips, M. M., & Terlevich, R. 1981, *PASP*, 93, 5
 Balestra, I., Mainieri, V., Popesso, P., et al. 2010, *A&A*, 512, A12
 Bannister, S. V. W., Stiavelli, M., Koekemoer, A. M., et al. 2006, *AJ*, 132, 1729
 Behrens, C., Dijkstra, M., & Niemeyer, J. C. 2014, *A&A*, 563, A77
 Binette, L., Groves, B., Villar-Martín, M., Fosbury, R. A. E., & Axon, D. J. 2003, *A&A*, 405, 9uisi75
 Borthakur, S., Heckman, T. M., Leitherer, C., & Overzier, R. A. 2014, *Science*, 346, 216
 Boutsia, K., Grazian, A., Giallongo, E., et al. 2011, *ApJ*, 736, 41
 Bouwens, R. J., Illingworth, G. D., Oesch, P. A., et al. 2015, *ArXiv e-prints*
 Brammer, G. B., Sánchez-Janssen, R., Labbé, I., et al. 2012, *ApJ*, 758, L17
 Bridge, C. R., Teplitz, H. I., Siana, B., et al. 2010, *ApJ*, 720, 465
 Brinchmann, J., Charlot, S., White, S. D. M., et al. 2004, *MNRAS*, 351, 1151
 Bruzual, G. & Charlot, S. 2003, *MNRAS*, 344, 1000
 Caccianiga, A. & Severgnini, P. 2011, *MNRAS*, 415, 1928
 Calzetti, D., Armus, L., Bohlin, R. C., et al. 2000, *ApJ*, 533, 682
 Calzetti, D., Kinney, A. L., & Storchi-Bergmann, T. 1994, *ApJ*, 429, 582
 Cardamone, C., Schawinski, K., Sarzi, M., et al. 2009, *MNRAS*, 399, 1191
 Cardamone, C. N., van Dokkum, P. G., Urry, C. M., et al. 2010, *ApJS*, 189, 270
 Cardelli, J. A., Clayton, G. C., & Mathis, J. S. 1989, *ApJ*, 345, 245
 Cassata, P., Le Fèvre, O., Charlot, S., et al. 2013, *A&A*, 556, A68
 Castellano, M., Fontana, A., Grazian, A., et al. 2012, *A&A*, 540, A39
 Cen, R. & Kimm, T. 2015, *ApJ*, 801, L25
 Christensen, L., Laursen, P., Richard, J., et al. 2012, *MNRAS*, 427, 1973
 de Barros, S., Reddy, N., & Shivaie, I. 2015, *ArXiv e-prints*
 De Brueck, C., Röttgering, H., Miley, G., van Breugel, W., & Best, P. 2000, *A&A*, 362, 519
 Domínguez, A., Siana, B., Henry, A. L., et al. 2013, *ApJ*, 763, 145
 Erb, D. K., Steidel, C. C., Shapley, A. E., et al. 2006, *ApJ*, 647, 128
 Ferland, G. J., Porter, R. L., van Hoof, P. A. M., et al. 2013, *Å*, 49, 137
 Finkelstein, S. L., Papovich, C., Dickinson, M., et al. 2013, *Nature*, 502, 524
 Fontana, A., Dunlop, J. S., Paris, D., et al. 2014, *A&A*, 570, A11
 Fontanot, F., Cristiani, S., Pfrommer, C., Cupani, G., & Vanzella, E. 2014, *MNRAS*, 438, 2097
 Förster Schreiber, N. M., Genzel, R., Bouché, N., et al. 2009, *ApJ*, 706, 1364
 Garnett, D. R., Shields, G. A., Peimbert, M., et al. 1999, *ApJ*, 513, 168
 Giallongo, E., Grazian, A., Fiore, F., et al. 2015, *A&A*, 578, A83
 Giavalisco, M., Ferguson, H. C., Koekemoer, A. M., et al. 2004, *ApJ*, 600, L93
 Gräfenr, G. & Vink, J. S. 2015, *A&A*, 578, L2
 Grazian, A., Fontana, A., Santini, P., et al. 2015, *A&A*, 575, A96
 Grogan, N. A., Kocevski, D. D., Faber, S. M., et al. 2011, *ApJS*, 197, 35
 Guo, Y., Ferguson, H. C., Giavalisco, M., et al. 2013, *ApJS*, 207, 24
 Hainline, K. N., Shapley, A. E., Greene, J. E., & Steidel, C. C. 2011, *ApJ*, 733, 31
 Hathi, N. P., Le Fèvre, O., Ilbert, O., et al. 2015, *ArXiv e-prints*
 Hayes, M., Östlin, G., Duval, F., et al. 2014, *ApJ*, 782, 6
 Heckman, T. M., Borthakur, S., Overzier, R., et al. 2011, *ApJ*, 730, 5
 Henry, A., Scarlata, C., Martin, C. L., & Erb, D. 2015, *ApJ*, 809, 19
 Holden, B. P., Oesch, P. A., Gonzalez, V. G., et al. 2014, *ArXiv e-prints*
 Inoue, A. K. & Iwata, I. 2008, *MNRAS*, 387, 1681
 Inoue, A. K., Shimizu, I., Iwata, I., & Tanaka, M. 2014, *MNRAS*, 442, 1805
 Iwata, I., Inoue, A. K., Matsuda, Y., et al. 2009, *ApJ*, 692, 1287
 James, B. L., Pettini, M., Christensen, L., et al. 2014, *MNRAS*, 440, 1794
 Jaskot, A. E. & Oey, M. S. 2013, *ApJ*, 766, 91
 Jaskot, A. E. & Oey, M. S. 2014, *ApJ*, 791, L19
 Jones, T., Stark, D. P., & Ellis, R. S. 2012, *ApJ*, 751, 51
 Jones, T. A., Ellis, R. S., Schenker, M. A., & Stark, D. P. 2013, *ApJ*, 779, 52
 Juneau, S., Bournaud, F., Charlot, S., et al. 2014, *ApJ*, 788, 88
 Juneau, S., Dickinson, M., Alexander, D. M., & Salim, S. 2011, *ApJ*, 736, 104
 Kashino, D., Silverman, J. D., Rodighiero, G., et al. 2013, *ApJ*, 777, L8
 Kennicutt, Jr., R. C. 1998, *ARA&A*, 36, 189
 Koekemoer, A. M., Faber, S. M., Ferguson, H. C., et al. 2011, *ApJS*, 197, 36
 Kulas, K. R., Shapley, A. E., Kollmeier, J. A., et al. 2012, *ApJ*, 745, 33
 Labbé, I., Oesch, P. A., Bouwens, R. J., et al. 2013, *ApJ*, 777, L19
 Lamareille, F., Mouhcine, M., Contini, T., Lewis, I., & Maddox, S. 2004, *MNRAS*, 350, 396
 Lanzuisi, G., Perna, M., Delvecchio, I., et al. 2015, *A&A*, 578, A120
 Leitherer, C. & Heckman, T. M. 1995, *ApJS*, 96, 9
 Lutz, D., Maiolino, R., Spoon, H. W. W., & Moorwood, A. F. M. 2004, *A&A*, 418, 465
 Ly, C., Malkan, M. A., Nagao, T., et al. 2014, *ApJ*, 780, 122
 Malkan, M., Webb, W., & Konopacky, Q. 2003, *ApJ*, 598, 878
 Maseda, M. V., van der Wel, A., Rix, H.-W., et al. 2014, *ApJ*, 791, 17
 Meurer, G. R., Heckman, T. M., & Calzetti, D. 1999, *ApJ*, 521, 64
 Mostardi, R. E., Shapley, A. E., Nestor, D. B., et al. 2013, *ApJ*, 779, 65
 Mostardi, R. E., Shapley, A. E., Steidel, C. C., et al. 2015, *ApJ*, 810, 107
 Nagao, T., Maiolino, R., & Marconi, A. 2006, *A&A*, 459, 85
 Nakajima, K. & Ouchi, M. 2014, *MNRAS*, 442, 900
 Nestor, D. B., Shapley, A. E., Kornei, K. A., Steidel, C. C., & Siana, B. 2013, *ApJ*, 765, 47
 Nestor, D. B., Shapley, A. E., Steidel, C. C., & Siana, B. 2011, *ApJ*, 736, 18
 Nonino, M., Dickinson, M., Rosati, P., et al. 2009, *ApJS*, 183, 244
 Oesch, P. A., van Dokkum, P. G., Illingworth, G. D., et al. 2015, *ApJ*, 804, L30
 Oke, J. B. & Gunn, J. E. 1983, *ApJ*, 266, 713
 Ono, Y., Ouchi, M., Mobasher, B., et al. 2012, *ApJ*, 744, 83
 Osterbrock, D. E. 1989, *Astrophysics of gaseous nebulae and active galactic nuclei*
 Pallottini, A., Ferrara, A., Pacucci, F., et al. 2015, *MNRAS*, 453, 2465
 Panessa, F., Bassani, L., Cappi, M., et al. 2006, *A&A*, 455, 173
 Pérez-Montero, E. 2014, *MNRAS*, 441, 2663
 Pope, A., Chary, R.-R., Alexander, D. M., et al. 2008, *ApJ*, 675, 1171
 Popesso, P., Dickinson, M., Nonino, M., et al. 2009, *A&A*, 494, 443
 Price, S. H., Kriek, M., Brammer, G. B., et al. 2014, *ApJ*, 788, 86
 Rauch, M., Becker, G. D., Haehnelt, M. G., et al. 2011, *MNRAS*, 418, 1115
 Reddy, N. A., Erb, D. K., Pettini, M., Steidel, C. C., & Shapley, A. E. 2010, *ApJ*, 712, 1070
 Reddy, N. A., Kriek, M., Shapley, A. E., et al. 2015, *ApJ*, 806, 259
 Roberts-Borsani, G. W., Bouwens, R. J., Oesch, P. A., et al. 2015, *ArXiv e-prints*
 Robertson, B. E., Ellis, R. S., Furlanetto, S. R., & Dunlop, J. S. 2015, *ApJ*, 802, L19
 Rousselot, P., Lidman, C., Cuby, J.-G., Moreels, G., & Monnet, G. 2000, *A&A*, 354, 1134
 Rujopakarn, W., Rieke, G. H., Papovich, C. J., et al. 2012, *ApJ*, 755, 168
 Salpeter, E. E. 1955, *ApJ*, 121, 161
 Santini, P., Fontana, A., Grazian, A., et al. 2009, *A&A*, 504, 751
 Schaerer, D. & de Barros, S. 2010, *A&A*, 515, A73+
 Scoville, N., Faisst, A., Capak, P., et al. 2015, *ApJ*, 800, 108
 Seaton, M. J. 1979, *MNRAS*, 187, 73P
 Shapley, A. E., Steidel, C. C., Pettini, M., & Adelberger, K. L. 2003, *ApJ*, 588, 65
 Shapley, A. E., Steidel, C. C., Pettini, M., Adelberger, K. L., & Erb, D. K. 2006, *ApJ*, 651, 688
 Shivaie, I., Reddy, N. A., Steidel, C. C., & Shapley, A. E. 2015, *ApJ*, 804, 149
 Siana, B., Shapley, A. E., Kulas, K. R., et al. 2015, *ApJ*, 804, 17
 Siana, B., Teplitz, H. I., Ferguson, H. C., et al. 2010, *ApJ*, 723, 241
 Smit, R., Bouwens, R. J., Franx, M., et al. 2015, *ApJ*, 801, 122
 Smit, R., Bouwens, R. J., Labbé, I., et al. 2014, *ApJ*, 784, 58
 Sobral, D., Matthee, J., Darvish, B., et al. 2015, *ApJ*, 808, 139
 Stark, D. P., Richard, J., Siana, B., et al. 2014, *MNRAS*, 445, 3200
 Stasińska, G., Izotov, Y., Morisset, C., & Guseva, N. 2015, *A&A*, 576, A83
 Steidel, C. C., Pettini, M., & Adelberger, K. L. 2001, *ApJ*, 546, 665
 Steidel, C. C., Rudie, G. C., Strom, A. L., et al. 2014, *ApJ*, 795, 165
 Storey, P. J. & Zeppen, C. J. 2000, *MNRAS*, 312, 813
 Szécsi, D., Langer, N., Yoon, S.-C., et al. 2015, *A&A*, 581, A15
 van der Wel, A., Straughn, A. N., Rix, H.-W., et al. 2011, *ApJ*, 742, 111
 Vanzella, E., de Barros, S., Castellano, M., et al. 2015, *A&A*, 576, A116
 Vanzella, E., Fontana, A., Pentericci, L., et al. 2014a, *A&A*, 569, A78
 Vanzella, E., Fontana, A., Zittr, A., et al. 2014b, *ApJ*, 783, L12
 Vanzella, E., Giavalisco, M., Inoue, A. K., et al. 2010a, *ApJ*, 725, 1011
 Vanzella, E., Guo, Y., Giavalisco, M., et al. 2012, *ApJ*, 751, 70
 Vanzella, E., Pentericci, L., Fontana, A., et al. 2011, *ApJ*, 730, L35
 Vanzella, E., Siana, B., Cristiani, S., & Nonino, M. 2010b, *MNRAS*, 404, 1672
 Verhamme, A., Orlitová, I., Schaerer, D., & Hayes, M. 2015, *A&A*, 578, A7
 Vignali, C., Alexander, D. M., Gilli, R., & Pozzi, F. 2010, *MNRAS*, 404, 48
 Windhorst, R. A., Cohen, S. H., Hathi, N. P., et al. 2011, *ApJS*, 193, 27
 Worseck, G., Prochaska, J. X., O'Meara, J. M., et al. 2014, *MNRAS*, 445, 1745

Yang, H., Malhotra, S., Gronke, M., et al. 2015, ArXiv e-prints
 Zackrisson, E., Inoue, A. K., & Jensen, H. 2013, ApJ, 777, 39
 Zitrin, A., Labbé, I., Belli, S., et al. 2015, ApJ, 810, L12

Appendix A: Emission lines dust correction

Emission lines are often dust corrected using the Balmer decrement ($H\alpha/H\beta$): the observed ratio between Balmer lines is compared with the expected ratio derived from theory (e.g., $H\alpha/H\beta = 2.86$; Osterbrock 1989), and assuming an attenuation curve, the dust correction is derived at any wavelength (e.g., Kashino et al. 2013; Domínguez et al. 2013; Price et al. 2014; Steidel et al. 2014). Unfortunately, regarding *Ion2*, the $H\alpha$ line is outside the MOSFIRE wavelength range and we must rely on the dust attenuation derived from the UV β slope ($f_\lambda \propto \lambda^\beta$; Meurer et al. 1999) or from SED fitting (which basically also relies on the fit of the UV β slope).

Calzetti et al. (2000) derive a relation between the stellar and nebular color excess as,

$$E(B - V)_{\text{nebular}} = 2.27 \times E(B - V)_{\text{stellar}}, \quad (\text{A.1})$$

and this relation is often misunderstood as both color excesses being derived with the same attenuation curve. Actually the nebular color excess is derived from a line-of-sight attenuation curve (e.g., Cardelli et al. 1989), while the stellar continuum color excess is derived with the Calzetti curve (Calzetti et al. 2000).

This issue is challenged by contradictory result about the stellar color excess relative to the nebular color excess at $z \sim 2$: some studies found results consistent with the misinterpretation described previously (e.g., Förster Schreiber et al. 2009), while other found $E(B - V)_{\text{nebular}} \sim E(B - V)_{\text{stellar}}$ (e.g., Erb et al. 2006; Reddy et al. 2010; Shivaee et al. 2015). A detailed comparison of a large sample of $z \sim 2$ star-forming galaxies observed with MOSFIRE and with measured Balmer decrement for most of this sample (Reddy et al. 2015), shows that the relation between $E(B - V)_{\text{nebular}}$ and $E(B - V)_{\text{stellar}}$ is in fact SFR (and sSFR) dependent (see also de Barros et al. 2015). To derive the emission line attenuation, we use the relation provided by Reddy et al. (2015):

$$E(B - V)_{\text{nebular}} - E(B - V)_{\text{stellar}} = -0.049 + 0.079 \times (\log(\text{sSFR}_{\text{SED}}) + 10) \quad (\text{A.2})$$

Reddy et al. (2015) emphasize that Equation A.2 is affected by a large scatter ($\sigma \sim 0.12$).

Appendix B: UV β slope and SED fitting procedure

We want to derive the UV β slope as accurately as possible because this quantity is known to be related to the dust attenuation, while also dependent on the age of the stellar population and the star formation history (Leitherer & Heckman 1995; Meurer et al. 1999). To derive the UV β slope, we perform a multi-band fitting, using the bands between 1500Å and 2500Å (Castellano et al. 2012). However, the flux in the z_{850} band is lower than what we expect from the observed fluxes in the band just blueward and redward z_{850} (I_{814} and Y_{098}). We compare theoretical expectation from the MOSDEF attenuation curve and the MW curve (Seaton 1979) with *Ion2* observed colors in Figure B.1. The MW curve exhibits the 2175Å bump which could explain the flux decrease in the z_{850} band, while uncertainties are too large to discriminate between a curve with or without the 2175Å bump. However, Scoville et al. (2015) report that their data are consistent with the

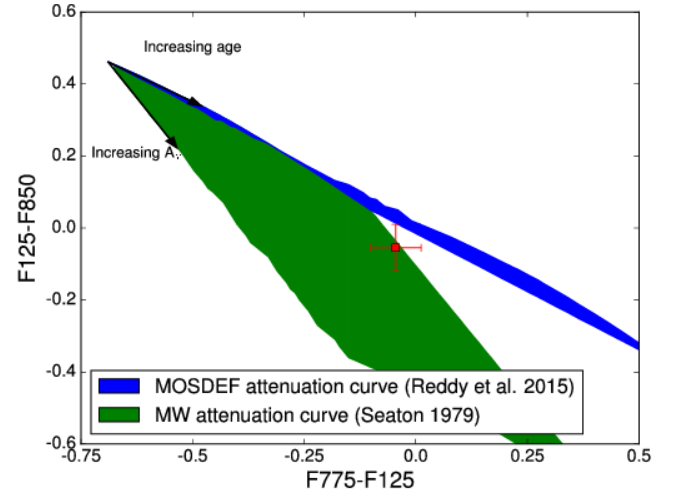


Fig. B.1. Range of F775–F125 and F125–F850 colors predicted with BC03 templates and the MOSDEF (Reddy et al. 2015) and MW attenuation curves (Seaton 1979). *Ion2* colors are shown with the red square.

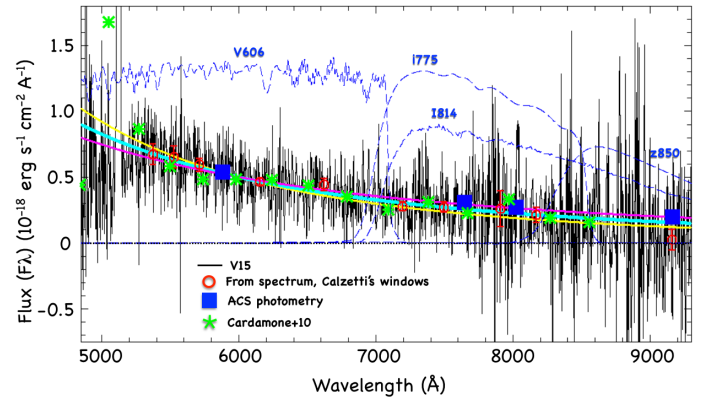


Fig. B.2. 1D UV spectrum from V15 (black). ACS photometry (blue squares) is shown along with the corresponding transmission curves (V_{606} , i_{775} , I_{814} , and z_{850} , blue dashed lines). We also show the medium band photometry from the MUSYC survey (green stars, Cardamone et al. 2010). The red dots and associated error bars show the flux derived through the wavelength windows used in Calzetti et al. (1994) to derive the UV β slope. The cyan line denotes the best fit over the Calzetti windows and the violet and yellow lines encompass the 68% uncertainty ($\beta = -2.75, -3.40$ and -2.20 , respectively).

presence of the 2175Å bump, while for Reddy et al. (2015) this presence is only marginal.

We derive the β slope from the UV spectrum, using the wavelength windows described in Calzetti et al. (1994), but excluding the 10th window because being outside the UV spectrum wavelength coverage. The median flux within each window is calculated and used to fit a linear relation in the observed spectrum, assuming the flux density per unit wavelength $F_\lambda \sim \lambda^\beta$, in units of $\text{erg s}^{-1} \text{cm}^{-2} \text{Å}^{-1}$ (Hathi et al. 2015). The resulting slope is $\beta = -2.75^{+0.55}_{-0.65}$. It is worth noting that the UV slope from the spectrum is not influenced by the possible 2175Å bump. The UV slope derived from the spectrum is consistent within 1σ with the β slope derived from multi-band fitting of the photometry (-2.20 ± 0.20).

Regarding the SED fitting procedure, we use BC03 templates (Bruzual & Charlot 2003) and we anchor the result to the UV β slope by not taking into account solutions inconsistent with the β slope derived from the UV spectrum, within 1σ . We also fix the metallicity to $Z = 0.2Z_{\odot}$, which is consistent with the metallicity derived in Section 3.2. We test different star formation histories (declining, rising, constant) and attenuation curves (Calzetti, MOSDEF, MW), assuming a Salpeter IMF (Salpeter 1955). The results show that the physical parameters such as the stellar mass and the age are not strongly affected by the assumptions. Therefore, in this work, we assume a constant star formation history and the MOSDEF attenuation curve. While the β slope is consistent with no or low dust attenuation, we use the relations derived in Reddy et al. (2015) to translate the β slope in color excess. This leads to $E(B - V)_{\text{stellar}} \leq 0.04$, while the Meurer relation (Meurer et al. 1999) leads to no dust attenuation because of the higher intrinsic β slope in this latter relation.